ARTICLE

Spectroscopic and Electrochemical Characterization of a Pr^{4+} Imidophosphorane Complex and the Redox Chemistry of Nd^{3+} and Dy^{3+} Complexes

Received 00th January 20xx,
Accepted 00th January 20xx

DOI: 10.1039/x0xx00000x

Natalie T. Rice[a†], Ivan A. Popov[bc‡], Rebecca K. Carlson[b], Samuel M. Greer[d], Andrew C. Boggiano [a], Benjamin W. Stein[d], John Bacsa[a], Enrique R. Batista[b]*, Ping Yang[b]*, Henry S. La Pierre[ae]*

The molecular tetravalent oxidation state for praseodymium is observed in solution via oxidation of the anionic trivalent precursor $[K][Pr^{3+}(NP(1,2\text{-bis-}^{t}Bu\text{-diamidoethane})(NEt_2))_4]$ (**1-Pr(NP*)**) with AgI at -35 °C. The Pr^{4+} complex is characterized in solution via cyclic voltammetry, UV-vis-NIR electronic absorption spectroscopy, and EPR spectroscopy. Electrochemical analyses of $[K][Ln^{3+}(NP(1,2\text{-bis-}^{t}Bu\text{-diamidoethane})(NEt_2))_4]$ (Ln = Nd and Dy) by cyclic voltammetry are reported and, in conjunction with theoretical modeling of electronic structure and oxidation potential, are indicative of principal ligand oxidations in contrast to the metal-centered oxidation observed for **1-Pr(NP*)**. The identification of a tetravalent praseodymium complex in *in situ* UV-vis and EPR experimensts is further validated by theoretical modeling of the redox chemistry and the UV-vis spectrum. The latter study was performed by extended multistate pair-density functional theory (XMS-PDFT) and implicates a multiconfigurational ground state for the tetravalent praseodymium complex.

Introduction

Molecular complexes of tetravalent lanthanides other than cerium were unknown until 2019.[1–7] The development of methodology to access uncommon lanthanide oxidation states in solution and as isolable complexes will change the toolkit to realize novel separations technologies including *f*-element ore processing and recycling[8,9] and spent nuclear fuel reprocessing.[10] The accessibility of uncommon lanthanide and actinide oxidation states also presents new opportunities for the design of quantum information technologies.[6,11–16]

Praseodymium and terbium were estimated to be the two most readily oxidized trivalent lanthanide ions after Ce with predicted $Ln^{3+/4+}$ potentials of +3.2 and +3.1 V versus NHE.[17] Neodymium and dysprosium are predicted to be more oxidizing, with their $Ln^{3+/4+}$ potentials at 4.4 and 4.9 V versus NHE, respectively.[6,17–19] The challenge in accessing these tetravalent ions as molecular complexes in solution is significant. It should be noted that tetravalent molecular ions in the gas phase (identified via mass spectrometry and/or vibrational spectroscopy in matrix isolation) have been observed for Pr, Nd, Tb, and Dy.[20–25] Remarkably, even Pr^{5+} has recently been observed in the gas phase.[23,26–29]

The recent isolation and characterization of tetravalent terbium and praseodymium complexes has shown that given the appropriate ligand field, the tetravalent oxidation state is accessible for lanthanides other than Ce. Our recent report of Tb^{4+} was achieved through oxidation of the trivalent imidophosphorane precursor, $[K][Tb^{3+}(NP^*)_4]$ where NP* = $(NP(1,2\text{-bis-}^{t}Bu\text{-diamidoethane})(NEt_2))^{1-}$ (**1-Tb(NP*)**) with AgI in diethyl ether or THF.[1] Mazzanti and co-workers have reported the isolation of two Tb^{4+} and one Pr^{4+} compounds, $[Tb^{4+}(OSi(O^{t}Bu)_3)_3(\kappa_2\text{-}OSi(O^{t}Bu)_3]$ and $[Ln^{4+}(OSiPh_3)_4(MeCN)_2]$ (Ln = Pr, Tb), using siloxide ligand frameworks.[2–4] Previous attempts to oxidize molecular Pr^{3+} complexes in solution have been documented, but have not resulted in the isolation or in the thorough in situ characterization of tetravalent praseodymium.[4,30,31] With the oxidation potential of $Pr^{3+/4+}$ estimated at just 0.1 V more oxidizing than Tb, and with **1-Tb(NP*)** having an oxidation potential of -0.72 V vs. Fc/Fc^{+} in THF (*vide infra*), it is reasonable to expect that the Pr^{3+} analogue, $[K][Pr^{3+}(NP^*)_4]$, **1-Pr(NP*)**, could be oxidized under similar conditions. Herein, we report the solution characterization (EPR, UV-vis-NIR, cyclic voltammetry, and theoretical analysis) of tetravalent praseodymium in the chemical oxidation of **1-Pr(NP*)**. Additionally, the cyclic voltammetric analysis of the corresponding trivalent Nd and Dy complexes $[K][Ln^{3+}(NP^*)_4]$ (Ln = Nd and Dy; **1-Nd(NP*)**, and **1-Dy(NP*)**) is described. This analysis is paired with theoretical modeling of these complexes' spectroscopic and redox properties to demonstrate the accessibility of Pr^{4+} and the

[a.] *School of Chemistry and Biochemistry, Georgia Institute of Technology, Atlanta, Georgia 30332-0400, United States..*
[b.] *Theoretical Division, Los Alamos National Laboratory, Los Alamos, New Mexico 87545, United States.*
[c.] *Department of Chemistry, The University of Akron, Akron, OH 44325-3601, United States.*
[d.] *Chemistry Division, Los Alamos National Laboratory, Los Alamos, New Mexico 87545, United States.*
[e.] *Nuclear and Radiological Engineering and Medical Physics Program, School of Mechanical Engineering, Georgia Institute of Technology, Atlanta, Georgia 30332-0400, United States*
† N.T.R. and I.A.P. contributed equally to this work.
Electronic Supplementary Information (ESI) available: [details of any supplementary information available should be included here]. See DOI: 10.1039/x0xx00000x

ligand properties driving these complexes' solution redox behavior. The detailed characterization of these oxidation processes – even if transient – is crucial to delineate the key aspects facilitating the stability of tetravalent lanthanide complexes.

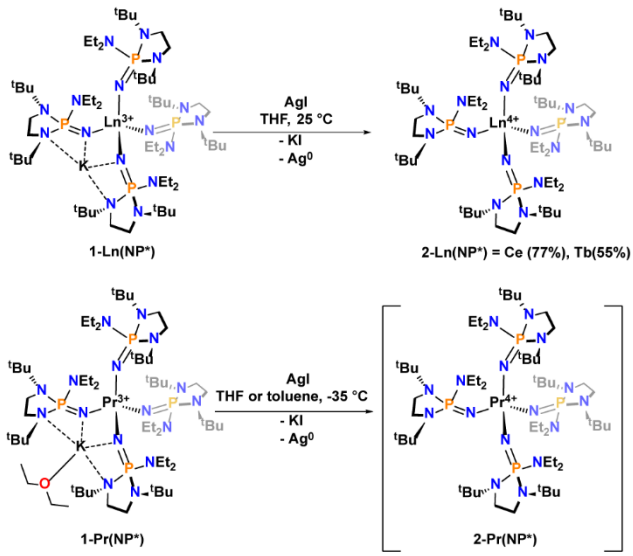

Scheme 1. (*top*) Previously reported syntheses of **2-Ce(NP*)** and **2-Tb(NP*)**. (*bottom*) Synthetic method for generation of **2-Pr(NP*)** in solution.

Results and discussion

The anionic, trivalent complexes, **1-Pr(NP*)**, **1-Nd(NP*)**, and **1-Dy(NP*)** were synthesized through a salt metathesis reaction with $LnI_3(THF)_x$ (x = 4 for La, Pr, 3.5 for Nd and Dy)[32] and four equivalents of the potassium salt of the ligand, $[NP^*]^{1-}$, **K(NP*)**, in diethyl ether.[1] Characterization of the trivalent complexes was performed by single crystal x-ray diffraction (SC-XRD), ^1H and $^{31}P\{^1H\}$ NMR, and UV-vis-NIR electronic absorption spectroscopy. In the solid-state, all three complexes are pseudotetrahedral and feature an inner-sphere potassium ion, for charge balance, bound by two of the ligands. These structures are very similar to the previously reported cerium, $[K][Ce^{3+}(NP^*)_4]$ (**1-Ce(NP*)**),[5] and terbium (**1-Tb(NP*)**)[1] analogues. The molecular structures for **1-Pr(NP*)**, **1-Nd(NP*)**, and **1-Dy(NP*)** are shown in ESI Figures S17-22 and important bond lengths and angles are tabulated in ESI Table S2. On average, the N–Ln–N bond angles are 109.4° for **1-Pr(NP*)**, **1-Nd(NP*)**, and **1-Dy(NP*)**. The Ln–N bond lengths for both the terminal ligands are slightly longer than the potassium bound ligands and both bond lengths shorten across the series from Pr to Dy, in line with the decrease in ionic radius[33] across the lanthanide series (ESI S15-16) and consistent with their trivalent oxidation state.

The solution characterization of the three complexes agrees well with the SC-XRD and the expected trivalent oxidation state. The $^{31}P\{^1H\}$ NMR spectra in C_6D_6 for **1-Pr(NP*)**, **1-Nd(NP*)**, and **1-Dy(NP*)** show a single observable resonance at 343.87, 525.93, and -2335.7 ppm, respectively. While two shifts are expected for the trivalent complexes due to the two different phosphorus environments in the solid-state (potassium capped and terminal ligands), one resonance is observed for all complexes in solution at room temperature, consistent with previous studies of **1-Ce(NP*)**.[5] In the case of **1-Pr(NP*)** in d_8-toluene, the single $^{31}P\{^1H\}$ resonance decoalesces into two broad signals at 717.51 and 444.95 ppm at -80 °C (See ESI Fig. S3) consistent with the model that the potassium is rapidly exchanging at room temperature in these complexes. The UV-vis-NIR electronic absorption spectra of **1-Pr(NP*)**, **1-Nd(NP*)**, and **1-Dy(NP*)** in THF are also consistent with the trivalent oxidation state for each metal ion and present characteristic f-f transitions (see ESI S31-33 for spectra and assignments).

The redox properties of these trivalent complexes were probed by cyclic voltammetry (0.1 M $[N(^nBu)_4][PF_6]$ in THF). The complex **1-Pr(NP*)** has an oxidation event that occurs at E_{pa} = -0.72 V vs Fc/Fc^+ at 200 mV/s. This oxidation event matches that observed for the isostructural **1-Tb(NP*)**, (E_{pa} = -0.72 V vs Fc/Fc^+, Fig. 1).† This similarity in the oxidation potential for **1-Pr(NP*)** and **1-Tb(NP*)** gives a primary indication that it is a metal centered oxidation. This observation is rooted in the agreement of previous experimental (aqueous and nonaqueous) and theoretical studies which placed the $Tb^{3+/4+}$ and $Pr^{3+/4+}$ oxidation potentials within 0.1 V of each other.[6,17,19,30] At slower scan rates (100-600 mV/s), no reduction event associated with the **1-Pr(NP*)** oxidation is observed. However, at higher scan rates, a reduction feature can be observed and is more prominent at higher scan rates (700-1200 mV/s, Fig. 1, ESI S23). The scan-rate dependence of the reduction event is suggestive of the instability of the oxidation product, $[Pr^{4+}(NP^*)_4]$ (**2-Pr(NP*)**), at room temperature. At 800 mV/s, the observed reduction event for **2-Pr(NP*)** occurs at approximately E_{pc} = -1.48 V vs Fc/Fc^+. It should also be noted that the large peak separation observed between the oxidation and reduction events for the **1-Ln(NP*)** and **2-Ln(NP*)** complexes points to a large kinetic barrier, potentially due to ligand reorganization energy.[34,35]

The cyclic voltammetry experiments for **1-Nd(NP*)** and **1-Dy(NP*)** diverge from what was found with **1-Tb(NP*)** and **1-Pr(NP*)**. For both **1-Nd(NP*)** and **1-Dy(NP*)** an oxidation is observed at E_{pa} = -0.43 V (Fig. 1), a ~300 mV shift from the potential observed for **1-Pr(NP*)** and **1-Tb(NP*)**. Based on the metal ion's predicted potentials at 4.4 and 4.9 versus NHE, the potentials of Nd^{3+} and Dy^{3+} are estimated to be 1.2 and 1.7 V more positive than that of Pr^{3+}, respectively, for a metal-centered oxidation. These oxidation events have no reduction associated with them even at higher scan rates (ESI S25-26) unlike in **1-Ce(NP*)**, **1-Tb(NP*)**, and **1-Pr(NP*)** and there is a significant decrease in observed current over subsequent sweeps of the potential, consistent with an irreversible redox event.

Additionally, control experiments were conducted with **K(NP*)** to examine the nature of the ligand oxidation potential and to benchmark the cyclic voltammetry studies of **1-Nd(NP*)** and **1-Dy(NP*)**. The ligand potassium salt, **K(NP*)**, has an irreversible oxidative event E_{pa} = 0.55 V vs Fc/Fc^+ (ESI S27). This

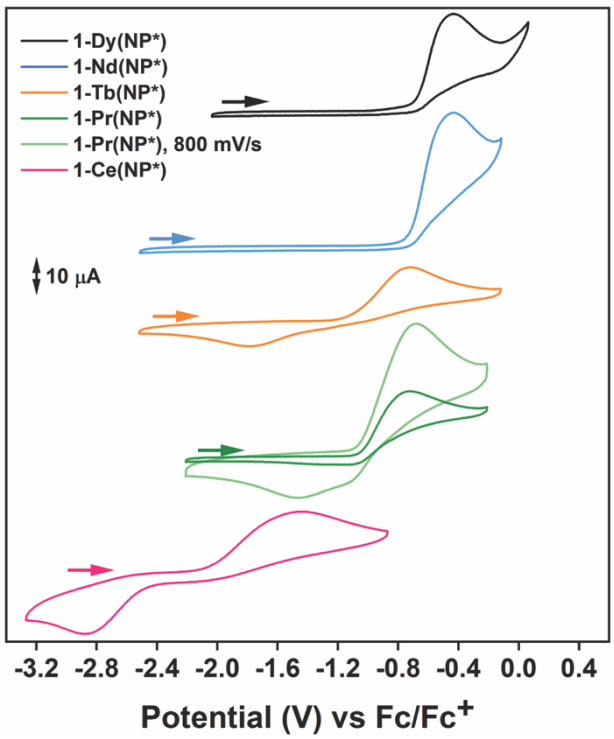

Figure 1. Scan rate dependent cyclic voltammograms of oxidation and reduction events of **1-Ln(NP*)** (where Ln = Ce, Pr, Nd, Tb, and Dy) versus Fc/Fc^+ (2.5 mM analyte, 0.1 M $[(^nBu_4)N][PF_6]$ in THF) at room temperature. For **1-Pr(NP*)**, a reduction event is observed beginning around 800 mV/s.

explains the inability to oxidize **K(NP*)** with AgI, where Ag^+ has an $E^{0\prime}$ of 0.41 V vs Fc/Fc^+ in THF.[36] In fact, the reaction of AgI and **K(NP*)** results in salt metathesis and the isolation of the silver salt of the imidophosphorane ligand, $[Ag_4[(NP^*)_4]$, **Ag(NP*)**.[37] The lack of a quasi-reversible feature for **1-Nd(NP*)** and **1-Dy(NP*)**, is in stark contrast to **1-Pr(NP*)** and **1-Tb(NP*)** and is indicative of a ligand-centered oxidation. It is important to note that the observed potential of **1-Nd(NP*)** and **1-Dy(NP*)** is 0.98 V more negative than that of **K(NP*).** This behavior is complementary to gas phase studies of tetravalent ions where, within a given ligand field, there is a break in the accessibility of the tetravalent state in the series of Ce, Pr, Tb, Nd, and Dy.[22,23,38] For example, the only accessible tetravalent complexes of the form $Ln^{4+}(OH)_4$ were Ce, Pr, Tb, and Dy and while tetravalent Nd was not observed.[38]

The observation of a reduction event for the oxidation product of **1-Pr(NP*)** at fast scan rates suggested that chemical oxidation may be feasible. Treating a pale green solution of **1-Pr(NP*)** at -35 °C in THF, diethyl ether, or toluene with AgI results in a dark blue solution over a period of 15 min to 1 hr, depending on the solvent choice (Scheme 1). When filtered filtered cold, grey powder (Ag^0) was observed on the pipet filter. This behavior parallels that of the oxidation of **1-Tb(NP*)** and **1-Ce(NP*)** with AgI. In the case of **1-Tb(NP*)**, the complex **2-Tb(NP*)** is formed and the reaction solution goes from colorless to deep indigo, but at room temperature.[1] For the oxidation of **1-Ce(NP*)**, the analogous $[Ce^{4+}(NP^*)_4]$ (**2-Ce(NP*)**) is formed and the reaction mixture shifts from yellow to deep red.[5] The low temperature oxidation of **1-Pr(NP*)** is anticipated to

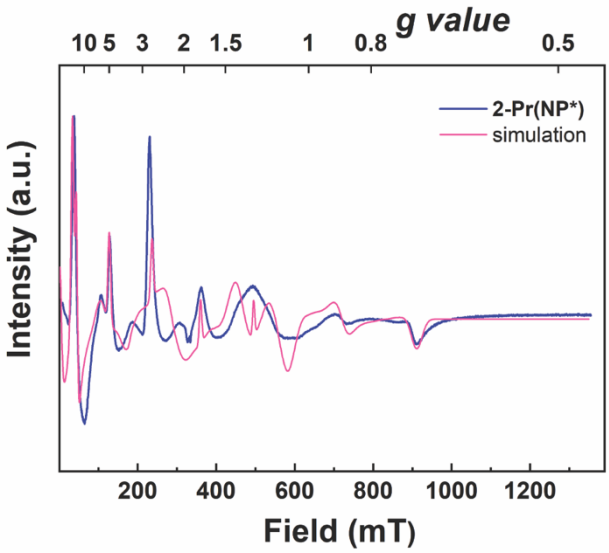

Figure 2. Experimental (*in situ*) (blue) and simulated (pink) X-band EPR spectrum of Pr^{4+} recorded at 9.37 GHz and 5 K in toluene. Simulation parameters: $g_z = 2.78$, $g_y = 1.41$, $g_x = 0.97$, $A_z = 4140$ MHz, $A_y = 2350$ MHz, and $A_x = 1680$ MHz.

behave analogously to these two reactions and give $[Pr^{4+}(NP^*)_4]$ (**2-Pr(NP*)**), as the initial oxidation product. The oxidation of **1-Pr(NP*)** can also be performed in *n*-pentane or hexanes with I_2 to immediately afford the same dark blue solution as observed with AgI. However, in congruence with the electrochemical measurements, **2-Pr(NP*)** is thermally unstable and decomposition occurs rapidly at room temperature, even in the absence of light.

The -45 °C $^{31}P\{^1H\}$ NMR spectrum of a solution of **2-Pr(NP*)** generated by oxidation of **1-Pr(NP*)** with AgI for 1 h. at -35 °C in d_8-toluene exhibits multiple signals: the primary constituents are the starting complex, **1-Pr(NP*)** (465.30 ppm at -45 °C), protonated ligand (33.67 ppm at -45 °C), and a new resonance at 13.93 ppm (ESI S14). This signal is attributed to **2-Pr(NP*)**. This temperature sensitive signal disappears completely when the sample was warmed to 0 °C concomitant with the loss of the dark blue color of the solution. These VT NMR studies indicate that the formation of **2-Pr(NP*)** is slow and decomposition reaction(s) are competitive, even at -35 °C which prevent the production of pure **2-Pr(NP*)** in solution and complicates purification and crystallographic characterization (as supported by bleaching of the reaction mixture while stored at -35 °C). Despite numerous attempts to obtain a crystal structure of **2-Pr(NP*)** via low temperature crystallization (down to -80 °C) and mounting, the conditions described above were unsuitable for the generation of XRD quality crystals. It should be noted that when the control reaction between **1-Pr(NP*)** and AgI is performed at *room temperature*, the only product observed in the $^{31}P\{^1H\}$ NMR is **Ag(NP*)**.[37] (Fig. S12-13). A similar salt metathesis is also observed at room temperature for reaction of **1-Nd(NP*)** and excess AgI (however this room temperature salt methasis reaction is not observed for **1-Ce(NP*)** and **1-Tb(NP*)**).

However, EPR spectroscopy facilitates the direct identification of tetravalent praseodymium in this reaction

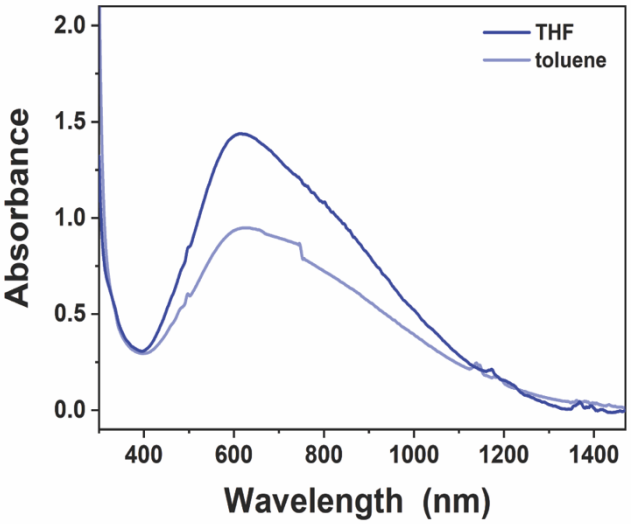

Figure 3. *In situ* UV-vis-NIR electronic absorption spectrum of a solution of **2-Pr(NP*)** at -30 ˚C in THF and -20 ˚C in toluene (see ESI for preparative details). The concentrations between the two solutions are not comparable. The discontinuity at ~750 nm is the grating change for this instrument window.

mixture (see ESI for preparative details). The solution of **2-Pr(NP*)** exhibits an X-band EPR spectrum at 5 K in toluene (Figure 2) that clearly identifies it as a Pr^{4+} complex. This signal is attenuated at 20 K and higher temperatures due to the fast spin-lattice relaxation and reduced Boltzmann polarization.[6,39] In modelling the observed spectrum, we assume that only lowest energy Kramers doublet is populated and, therefore, we use an effective spin-$^1/_2$ system to model the $J = {}^5/_2$ ground state of the Pr^{4+} in solution. The X-band EPR spectrum was analyzed within the framework of a standard spin Hamiltonian:

$$\hat{\mathrm{H}}_{\mathrm{spin}} = \beta_e \vec{\mathbf{B}} \cdot \tilde{\boldsymbol{g}} \cdot \hat{\mathbf{S}} - g_n \beta_n \vec{\mathbf{B}} \cdot \hat{\mathbf{I}} + \hat{\mathbf{S}} \cdot \tilde{\mathbf{A}} \cdot \hat{\mathbf{I}}$$

where β_e is the Bohr magneton, $\vec{\mathbf{B}}$ is the magnetic field vector, $\tilde{\boldsymbol{g}}$ is the *g*-tensor, $\hat{\mathbf{S}}$ is the total electronic spin operator, $\tilde{\mathbf{A}}$ is the electro-nuclear hyperfine coupling tensor, g_n is the nuclear gyromagnetic ratio (g_n = 1.71 for ^{141}Pr), β_n is the nuclear magneton, and $\hat{\mathbf{I}}$ is the nuclear spin ($I = {}^5/_2$ for ^{141}Pr). To reduce the number of parameters, $\tilde{\boldsymbol{g}}$ and $\tilde{\mathbf{A}}$ are assumed to be collinear and that the quadrupole interaction is negligible.

The combination of *g*-anisotropy and large hyperfine coupling makes the EPR spectrum of Pr^{4+} difficult to interpret. Under zero magnetic field an effective $S = ½$ system will exhibit a total nuclear and electron spin angular momentum, *F*, that can couple either ferromagnetically ($F = I + S$) or antiferromagnetically ($F = |I - S|$). In the case of Pr^{4+} ($I = {}^5/_2$, $S_{\mathrm{eff}} = {}^1/_2$), *F* will take on values of 2 and 3 with $F = 2$ lying lowest in energy. As the applied magnetic field is increased, the m_F sublevels (m_F = -*F*, -*F*+1, …, *F*) will separate and eventually when $\beta_e \vec{\mathbf{B}} \cdot \tilde{\boldsymbol{g}}$ is large compared to $\hat{\mathbf{S}} \cdot \tilde{\mathbf{A}} \cdot \hat{\mathbf{I}}$ the states will separate into two groups, one with $m_s = -{}^1/_2$ and the other with $m_s = ½$. The transition between low ($|F,m_F\rangle$) and high ($|S,I,m_S,m_I\rangle$) field limits is shown schematically in Figure S29. At the field used in this EPR experiment the high field limit is not reached, and the states exist in-between those best described by $|F,m_F\rangle$ and the regime where the $|S,I,m_S,m_I\rangle$ state label is best used. In practice this means that adjusting an individual component of the $\tilde{\mathbf{A}}$-tensor will simultaneously affect the energy levels of *all* molecular orientations.

Given these constraints, the experimental spectrum was fit under the assumption that the peak observed at the highest field (~910 mT) corresponds to the final allowed transition, *i.e.* no transitions at higher fields exist. We chose the frame of our *g*-values such that the smallest *g*-value is g_x, the intermediate value is g_y and the largest *g*-value is g_z. In this frame, we assign the transition occurring at the highest field (assumed to be the final allowed transition) as $|m_S = -{}^1/_2, m_I = -{}^5/_2\rangle \rightarrow |m_S = +{}^1/_2, m_I = -{}^5/_2\rangle$ where the magnetic field vector is parallel to g_x. Others have noted that the ratio g_i/A_i is similar for all three components, we can therefore assign the second highest field peak (~720 mT) as the transition between $|m_S = -{}^1/_2, m_I = -{}^5/_2\rangle \rightarrow |m_S = +{}^1/_2, m_I = -{}^5/_2\rangle$ with the magnetic field oriented along g_y. Unfortunately, even with these assignments in place the fact that the parameters cannot be efficiently separated still remains. Our procedure for simulating the spectrum was to vary the g_z and A_z components while simultaneously varying g_x/A_x and g_y/A_y to ensure that the above transitions are correctly reproduced. Ultimately, our best simulation parameters were: $g_z = 2.78$, $g_y = 1.41$, $g_x = 0.97$, $A_z = 4140$ MHz, $A_y = 2350$ MHz, and $A_x = 1680$ MHz.

Several previous EPR studies of Pr^{4+} doped into various oxides have reported *g*-values between 0.55 and 1.27.[6,40–46] Most of these previously reported species exist in an octahedral geometry. The significant difference in our observed *g* – values can be rationalized by a different coordination geometry in this study versus previous studies. Here, the Pr^{4+} resides in a distorted T_d ligand field that effectively inverts the ligand field potential relative to an octahedral environment (Figure S30). This means that while the ground state of the previously reported Pr^{4+} species were Γ_7 doublets, here, the ground state is a quadruplet Γ_8. Given the deviation from ideal T_d symmetry we can expect that the quadruplet Γ_8 will split and that the composition of the resulting Kramers doublet will be very sensitive to the distortion. It should be noted that no X-band EPR spectrum was observed for the f^2, Pr^{3+} precursor, **1-Pr(NP*)**.

The UV-vis-NIR electronic absorption spectrum for a solution of **2-Pr(NP*)** (see ESI for preparative details) in toluene shows a broad absorption feature with a maximum of 613 nm that extends from 1300-400 nm at -20 °C as shown in Figure 3. This broad absorption feature is analogous to the UV-vis-NIR absorption spectrum of the deep purple complex **2-Tb(NP*)**, which has an absorption feature with a maximum at 575 nm and stretching ~1150-400 nm. The absorption spectrum for **2-Pr(NP*)** is drastically different from that of **1-Pr(NP*)** which only reveals, at high concentration, the characteristic f-f transitions of the $4f^2$, Pr^{3+} ion. These observations are also in line with early studies of tetravalent Pr and Tb in aqueous solution which displayed large absorption features upon oxidation of concentrated carbonate and/or hydroxide solutions via electrolysis (450-250 nm, λ_{max} = 283 nm) and with $[Pr^{4+}(OSiPh_3)_4(MeCN)_2]$ which produces a similarly shaped UV-

Table 1. Comparison of the theoretical (Theor) and experimental (Exp) reduction potentials (V). Calculated vertical and adiabatic detachment energy (VDE and ADE), as well as vertical and adiabatic electron affinity (VEA and AEA) are both included. The nature of the redox events is shown in square brackets indicating metal-based [M] or ligand-based [L] oxidations.

Complex/ potential	E_{pa} oxidation potential			E_{pc} reduction potential		
	Exp	Theor VDE*	Theor ADE^	Exp	Theor VEA**	Theor AEA^^
1-Pr(NP*)/2-Pr(NP*)	-0.72	-0.58 [L]	-0.93 [M]	-1.48	-1.68 [M]	-0.99 [M]
1-Nd(NP*)/2-Nd(NP*)	-0.43	-0.52 [L]	-0.87 [L]	N/A	-1.32 [L]	-0.78 [L]
1-Dy(NP*)/2-Dy(NP*)	-0.43	-0.46 [L]	-0.68 [L]	N/A	-1.11 [L]	-0.70 [L]

*VDE stands for vertical detachment energy calculated as the energy difference between that of [**1-Ln(NP*)**] and its oxidized counterpart [**1-Ln(NP*)**]$^+$, which has the geometry of **1-Ln(NP*)**.

^ADE stands for adiabatic detachment energy calculated as the energy difference between that of **1-Ln(NP*)** and its oxidized counterpart [**1-Ln(NP*)**]$^+$, the geometry of which was fully optimized.

VEA stands for vertical electron affinity calculated as the energy difference between that of **2-Ln(NP*) and its reduced counterpart [**2-Ln(NP*)**]$^-$, which has the geometry of **2-Ln(NP*)**.

^^AEA stands for adiabatic electron affinity calculated as the energy difference between that of **2-Ln(NP*)** and its reduced counterpart [**2-Ln(NP*)**]$^-$, the geometry of which was fully optimized.

vis spectrum in THF spanning 700-275 nm with a λ_{max} = 363 nm.[4,30] It should be noted that the measurements for $[Pr^{4+}(OSiPh_3)_4(MeCN)_2]$ had to be performed immediately after dissolution because of complex instability in THF at room temperature. The maximum for **2-Pr(NP*)**, however, is shifted to lower energy in comparison to the aforementioned Pr^{4+} studies in line with nitrogen rather than oxygen-based donor atoms. Please see the theoretical section for further discussion of the origin of the transitions observed for **2-Pr(NP*)**.

Theoretical Studies

Density functional theory (DFT) and multi-reference calculations (XMS-PDFT) were performed to interpret UV-vis spectra and to study the redox processes of the Pr, Nd, and Dy complexes. The first-principles calculations reveal fundamental differences in the geometric and electronic structures from the molecular orbital and chemical bonding perspectives (see the Supporting Information file for complete details of the computational methodology).

The computed structural metrics for the lowest energy spin states, triplet for **1-Pr(NP*)**, quartet for **1-Nd(NP*)**, and sextet for **1-Dy(NP*)**, are in good agreement with the SC-XRD data, with Ln–N and N–P bond distances, as well as Ln–N–P and N–Ln–N valence angles deviating by less than 1.1%, 0.5%, 4.1%, and 0.3% of the experimental parameters, respectively, providing confidence in the theoretical model (Table S12). The Ln–N bond distances in **1-Ln(NP*)** (Ln=Pr, Nd, Dy) are indicative of the trivalent oxidation state of the metal centers.[33] In accordance with the metal-based oxidations reported for the similar $Ce^{3+/4+}$ and $Tb^{3+/4+}$ complexes[1,5] and the contraction of the metal ionic radii in $Ln^{3+/4+}$,[33] the Pr–N bond distances in **2-Pr(NP*)** are shorter than those in **1-Pr(NP*)** on average by 0.147 Å (Table S13), supporting the Pr^{4+} oxidation state in **2-Pr(NP*)**. In contrast, the Ln–N bonds in **2-Nd(NP*)** and **2-Dy(NP*)** do not contract similarly upon oxidation. Three of the Ln–N bond distances (Table S13) in the oxidized compounds of Nd and Dy are almost identical to those in their trivalent counterparts (contracted by ~0.05-0.06 Å): 2.318 Å in **1-Nd(NP*)** vs. 2.258 A in **2-Nd(NP*)**, and 2.215 Å in **1-Dy(NP*)** vs. 2.168 Å in **2-Dy(NP*)**. Additionally, in **2-Nd(NP*)** and **2-Dy(NP*)**, one of the four Ln–N bond distances elongates significantly by ~0.14-0.16 Å. This pattern is in contrast to that observed for **2-Pr(NP*)** in which all four Ln–N bond distances contract by ~0.15 Å in comparison to **1-Pr(NP*)**. This supports the qualitatively different nature of oxidation experimentally observed for **1-Pr(NP*)** *vs.* for **1-Nd(NP*)/1-Dy(NP*)**, *i.e.* metal-based vs. ligand-based oxidations, respectively.

Theoretical E_{pa} and E_{pc} redox potentials of the Pr, Nd, and Dy complexes (Table 1) computed by considering two possible routes, *i.e.* metal- and ligand-centered oxidations/reductions, may also help identify the differences between the corresponding complexes of Pr and Nd/Dy. The electron detachment from **1-Nd(NP*)** and **1-Dy(NP*)** computed as the vertical detachment energy (VDE) (*i.e.* when the geometry of the **1-Ln(NP*)** species is the same as that of the oxidized counterparts), yields the values of -0.52 V and -0.46 V, respectively. These values describe ligand-based oxidations (Ln^{3+} is preserved in both oxidized compounds) and match well the experimental E_{pa} value of -0.43 V measured for these compounds. Geometry relaxation associated with the ligand oxidation of **1-Nd(NP*)** and **1-Dy(NP*)** leads to one of the Ln–N bonds elongating and slightly contracting the other three, producing structures similar to those of **2-Nd(NP*)** and **2-Dy(NP*)**. These structural relaxations computed as adiabatic detachment energies (ADEs) (*i.e* when geometries of **1-**

Nd(NP*)/1-Dy(NP*) and their oxidized counterparts are relaxed), correspond to the appreciably more negative values of -0.87 V and -0.68 V, respectively. This indicates that the experimental oxidation potential reflects the process of instantaneous electron detachment before the structural reorganization, and that this oxidation is ligand-based.

The electron detachment from **1-Pr(NP*)** before geometry relaxation favors a ligand-based oxidation with a VDE of -0.58 V. Relaxing the oxidized geometry induces a metal-to-ligand electron transfer yielding a metal-oxidized compound and a total energy difference of -0.93 V. In this case, the Pr–N metal bond contraction is the major structural change occurring upon electron detachment from the Pr center accounting for the Pr–N bond contraction by ~0.14 Å. Both VDE and ADE values are close to the experimental E_{pa} value of -0.72 V, making it hard to conclusively state the nature of the **1-Pr(NP*)** oxidation based on these values alone.

The theoretical reduction potential E_{pc} of the **2-Pr(NP*)** complex was calculated based on the energy difference between that of **2-Pr(NP*)** and its reduced counterpart possessing the geometry of **2-Pr(NP*)** (without geometry relaxation), brings the vertical electron affinity (VEA) value of -1.68 V, which is also very close to the experimental E_{pc} value of -1.48 V. Hence, the experimental E_{pc} reflects a reduction potential upon instantaneous electron addition. The structural relaxation upon the reduction of **2-Pr(NP*)** elongates all Pr–N bonds to the average of 2.327 Å, in agreement with the Pr^{3+} species, producing the adiabatic electron affinity (AEA) value of -0.99 V (Table 1).

The fundamentally different behavior of the Ln^{3+} (Ln=Pr vs. Nd/Dy) complexes upon oxidation can be rationalized via molecular orbital (MO) level diagrams, which show different positions of the 4f-dominant MOs with respect to the HOMO level in **1-Pr(NP*)** *vs.* **1-Nd(NP*)/1-Dy(NP*)** (Figure S34). In all complexes, the frontier occupied orbitals are dominated by the ligand contributions with the metal 4f orbitals residing lower in energies to various degrees. It is easier to oxidize the lanthanide the closer its 4f-dominant orbitals are to the HOMO level, as is the case for the **1-Ce(NP*)** complex. In **1-Pr(NP*)**, the 4f-dominant orbital is 0.49 eV below HOMO rendering it available for oxidation. In **1-Tb(NP*)**, this difference was slightly larger, 0.65 eV, but it was still a metal-based oxidation.[1] In contrast, in **1-Nd(NP*)** and **1-Dy(NP*)**, the highest 4f dominant MO of the metal is located deeper in energy, *i.e.* 2.00 eV and 0.85 eV lower than HOMO, respectively, complicating the removal of an electron from the metal. In principle, the energy of the 4f dominant MOs with respect to HOMO could be successfully used as a general guideline for the prediction of the nature of oxidation in similar complexes featuring other Ln metals. However, it is important to note that it is hard to determine the absolute cut-off value to predict whether a metal or a ligand would lose an electron upon oxidation as the removal of an electron will lead to the relaxation of all the nearby levels as they are all coupled in the functional. From this work we come up with a rule-of-thumb that the transition from metal-centered to ligand-centered oxidation for these complexes occurs when the highest occupied 4f dominant MO of Ln is between 0.65 and 0.85 eV from the HOMO level.

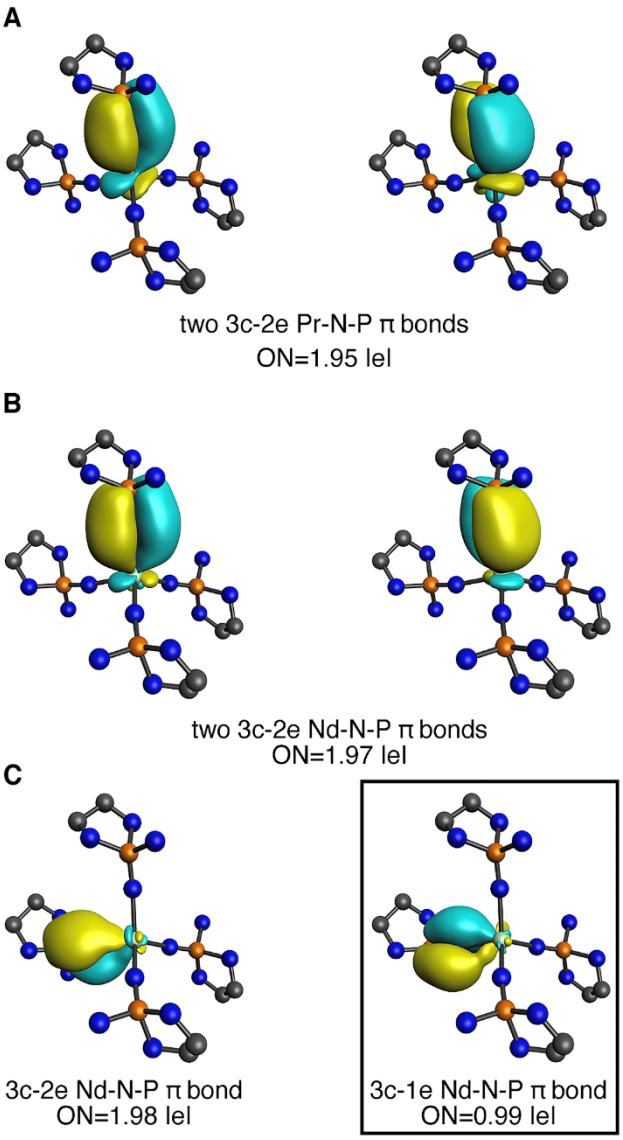

Figure 4. Comparison of the Ln–N–P π interactions in **2-Pr(NP*)** vs. **2-Nd(NP*)**. (A) Two 3c–2e Pr–N–P π bonds identified for one ligand. An equivalent set of bonds was found for other three ligands. (B) Two 3c–2e Nd–N–P π bonds identified for one of the three shorter Nd–N contacts. An equivalent set of bonds was found for other two ligands. (C) Two Nd–N–P π bonds identified for the longer Nd–N contact. H atoms and side groups of the ligands (^{t}Bu, Et_2) are omitted for simplicity. ON stands for the occupation number, and is equal to 2.00 |e| and 1 .00 |e| in an ideal case for a doubly- and singly occupied bond, respectively.

To understand the difference in geometric and electronic structures between the **2-Pr(NP*)** and **2-Nd(NP*)/2-Dy(NP*)** complexes, a chemical bonding analysis was performed. According to the natural bond orbital (NBO) analysis, similar elements of chemical bonding were found in **2-Pr(NP*)** as in the previously reported valence isoelectronic **1-Ce(NP*)**.[5] Specifically, there is formally one unpaired electron accounting for the $4f^1$ configuration of the Pr^{4+} species, *i.e.* one-center, one-electron α NBO (1c–1e α NBO, 99.91% f-character, Figure S39A) that stems from the 4f-dominant HOMO-20 (69% Pr, Figure

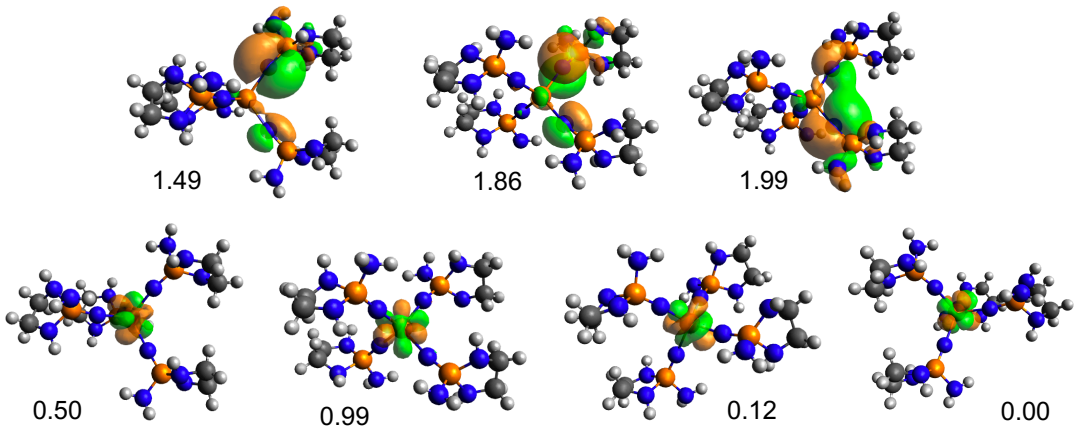

Figure 5. Selected natural orbitals from active space 1 (AS1) of **2-Pr(NP*)** with natural orbital occupation numbers for the 1st reference state that contributes to the XMS-PDFT ground state eigenvector.

S37). Similar to **1-Ce(NP*)**, the Pr–N bonding in **2-Pr(NP***) is described by four 2c–2e (two-center, two-electron) Pr–N σ bonds (one per each ligand, Figure S39B) and eight 3c–2e Pr–N–P π bonds (two per each ligand, Figure 39B), all highly polarized towards N atoms (Table S16).

The qualitative NBO picture (*i.e.* the number and type of the bonds) of **1-Pr(NP*)** is similar to that of **2-Pr(NP*)** for both Pr–N σ and Pr–N–P π bonds, though instead of one unpaired f-electron, there are two of them (two 1c–1e α NBOs, 99.88% f-character), as expected for the $4f^2$, Pr^{3+} species (Table S14, Figure S41). The difference is also noted in the polarization of the bond and hybridization. Similar to the analogous Ce^{3+}/Ce^{4+} and Tb^{3+}/Tb^{4+} complexes,[1,5] larger contributions of the Pr atom in the Pr–N σ and Pr–N–π bonds are found in the tetravalent state than in the trivalent one (by 4.43% for σ and 3.33% for π, Table S16), in accordance with the significantly shorter Pr–N bonds in **2-Pr(NP*)**. Likewise, the f-character in the Pr NBO hybrids is significantly higher in **2-Pr(NP*)** than in **1-Pr(NP*)**, *i.e.* 33.03% vs. 27.11% for σ bonds, and 67.31% vs. 64.16% for π bonds, respectively (Table S18). Overall, the greater contribution of Pr orbitals in the Pr–N bonding as well as the larger participation of 4f electrons accounts for the stronger covalent interactions in **2-Pr(NP*)** as compared to **1-Pr(NP*)**.

Due to the similarities in the geometric and electronic structures of the Nd and Dy complexes, the NBO results only for the **1-Nd(NP*)**/**2-Nd(NP*)** species are discussed further (see the Supporting Information for the NBO results of the Dy counterparts). In contrast to **2-Pr(NP*)**, **2-Nd(NP*)** does not show stronger Ln–N covalent interactions in comparison to its trivalent counterpart (Tables S16-19). In fact, the average bond polarization of the Nd–N σ and Nd–N–P π bonds is very similar between **1-Nd(NP*)** and **2-Nd(NP*)** with 5.61% vs. 5.89% Nd participation in the σ bond and 1.13% vs. 1.41% for π, respectively. This is in line with the almost equal average Ln–N bond distances found in **1-Ln(NP*)** and **2-Ln(NP*)** for Nd and Dy. In both **1-Nd(NP*)** and **2-Nd(NP*)** NBO found three unpaired f-electrons on Nd (three 1c–1e α NBOs, 99.95% f-character), which are very localized with occupation numbers (ON) of 0.98-1.00 |e| (Figure S42A). This result is indicative of the Nd^{3+} oxidation state in both complexes.

While the Nd–N σ bonding framework is qualitatively the same in **1-Nd(NP*)** and **2-Nd(NP*)**, *i.e.* one 2c–2e Nd–N σ bond per ligand (Figure S42B), the π bonding changes upon oxidation. One of the eight 3c–2e Nd–N–P π bonds becomes singly occupied, *i.e.* 3c–1e bond with ON=0.99 |e| is formed (Figure 4C) instead of one of the 3c–2e π bonds. It is found that upon oxidation ~80% of the electron density associated with one of the ligand-dominant α MO is lost from N 2p orbital and ~20% from the orbitals of P and neighboring atoms. This explains the significant elongation of one of the Nd–N bonds (2.474 Å), while three other bonds slightly shrink upon oxidation by ~0.06 Å. The longest Nd–N distance in **2-Nd(NP*)** shows the smallest Nd contribution in both Nd–N σ and Nd–N–P π bonds as compared to other three shorter bonds: 4.08% vs. 6.49% for σ bonds, and 0.60% vs. 1.68% for π bonds, respectively (Table S17). On average, the 4f contribution of Nd in these bonds in **2-Nd(NP*)** is similar to that of **1-Nd(NP*)**: 27.00% vs. 26.03% for σ bonds, and 51.66% vs. 53.00% for π bonds, respectively (Tables S18-19). Overall, due to the ligand-based oxidation, distinctly different geometric structures are formed in **2-Nd(NP*)**/**2-Dy(NP*)** in comparison to metal-oxidized **2-Pr(NP*)**, **2-Ce(NP*)**, and **2-Tb(NP*)**.[1,5] Significantly less covalent Ln–N bonding interactions are found in **2-Nd(NP*)/2-Dy(NP*)** as compared to **2-Pr(NP*)** due to the smaller Nd and Dy contributions to these bonds and smaller 4f character of the corresponding Nd and Dy NBO hybrids, which are reminiscent of those in **1-Nd(NP*)/1-Dy(NP*).**

UV-vis spectra of the **1-Ln(NP*)** (Ln=Pr, Nd, Dy) complexes (Figure S35) using TDDFT show electronic excitations primarily in the higher energy region (~290nm and higher), although it is also important to note that the f-f transitions observed experimentally were not reproduced at the TDDFT level, suggesting the need for multireference treatment to more accurately characterize the wave functions of these states. According to the natural transition orbital (NTO) analysis, the excitations above 300 nm in all **1-Ln(NP*)** complexes can be

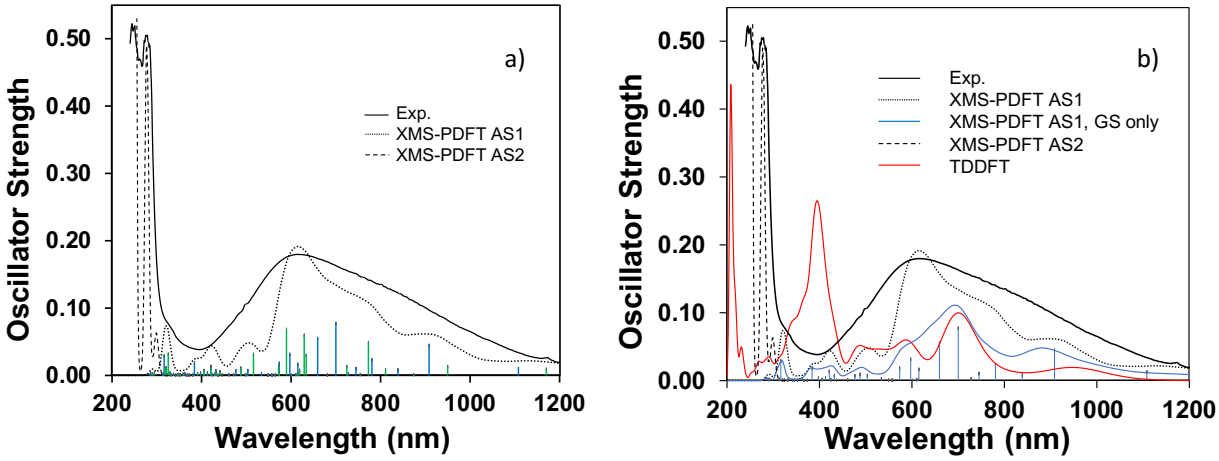

Figure 6. a) Experimental UV-Vis-NIR spectrum of **2-Pr(NP*)** scaled by 0.12 to match XMS-PDFT intensities and the computed XMS-PDFT spectrum (unshifted) up to 300 nm using the ftLSDA on-top functional (dotted line). The blue sticks are the oscillator strengths for transitions from the ground state and the green sticks are oscillator strengths for transitions from the nearly degenerate state that is about 0.06 eV above the ground state. The dashed line is the XMS-PDFT spectrum for the highest energy region, red shifted by 35 nm. AS1 and AS2 refer to active space 1 and active space 2, respectively (see SI). b) Same as a) but with TDDFT in red and XMS-PDFT spectrum from ground state (GS) only in blue.

primarily described as a mixture of the ligand-to-ligand (LLCT) and ligand-to-metal (LMCT) charge transfer excitations. In addition, metal-to-ligand (MLCT) excitations occur at higher energy, starting at ~245nm in **1-Pr(NP*)** and at ~220nm in **1-Dy(NP*)**, and these MLCT are absent in **1-Nd(NP*)** in the considered energy range up to ~200nm, in line with the significantly lower in energy 4f dominant MOs of Nd.

The TDDFT spectra of the **2-Nd(NP*)** and **2-Dy(NP*)** complexes (Figure S38) are similar to each other. The smaller HOMO-LUMO gaps (Figure S37) in **2-Nd(NP*)** (1.35 eV) and **2-Dy(NP*)** (1.28 eV) in comparison to that in **2-Pr(NP*)** (2.82 eV) facilitate excitations in the lower energy region, emerging at ~2400 nm. Analysis with NTO reveals similar electronic excitations in both **2-Nd(NP*)** and **2-Dy(NP*)** within the considered range of ~200-2400 nm. For brevity, TDDFT results of **2-Nd(NP*)** are discussed here, and those of **2-Dy(NP*)** in the Supporting Information. Specifically, the broad band at ~840-2500 nm in **2-Nd(NP*)** is dominated by the LLCT excitations arising from the 5 frontier ligand-dominant MOs (primarily 2p orbitals of N atoms) to the LUMO, which is also ligand-dominant. The band at the ~420-750 nm range features similar LLCT excitations, with additional MLCT excitations and f-f transition. LMCT excitations start appearing at 306 nm and higher in energy, in addition to the LLCT excitations.

Qualitatively different MO diagrams of **2-Nd(NP*)/2-Dy(NP*)** and **2-Pr(NP*)** (Figure S37) support the different nature of their excitations producing distinct TDDFT spectra. In order to accurately model the UV-vis spectrum of **2-Pr(NP*)**, we used multiconfiguration pair-density functional theory (MC-PDFT)[47], using the extended multistate pair-density functional theory (XMS-PDFT)[48] variant with the ftLSDA[49] on-top functional. With XMS-PDFT, two nearly degenerate states, 0.06 eV apart, are found that are linear combinations of equal weight of the 1st and 3rd reference states. These reference wave functions have the occupation $(L)^{1.5}(L)^{1.9}(L)^{2.0}(f)^{0.5}$ $(f)^{1.0}(f)^{0.1}(f)^{0.0}$ (Figure 5), where L is a ligand orbital and f is a lanthanide 4f orbital. The two configurations differ only in which f orbitals are occupied. Due to the more covalent nature of the Pr–N bond, there is a partial hole in the ligand shell, creating a more complicated electronic structure than a purely f^1 system. This electronic structure is another tantalizing example of multiconfigurational behavior in the spectroscopy of tetravalent lanthanides and is an important area for further study.[6,50–52]

The result of this more complicated ground state electronic structure is that the UV-vis spectrum can only be modeled accurately by accounting for excitations from both nearly degenerate low energy states with XMS-PDFT. The simulated XMS-PDFT spectrum is shown in Figure 6A, where we used two slightly different active spaces (see Figures S43 and S44) to model the 300-1200 nm range and the 200-300 nm range. The XMS-PDFT result is in excellent agreement with experiment, where the transitions in the 300-1200 nm range are ligand to metal with some f-f component, and the transitions in the 200-300 nm range additionally include ligand to ligand excitations.

Comparing XMS-PDFT to TDDFT for **2-Pr(NP*)**, the transitions from the XMS-PDFT ground state only, correspond well with the TDDFT transitions in the 500-1200 nm range (Figure 6B). The XMS-PDFT transitions are clustered under the TDDFT peaks in this region. These TDDFT excitations are dominated by LMCT, which is similar to the XMS-PDFT assignment. Similar transitions were reported earlier for the **2-Ce(NP*)** and **2-Tb(NP*)** complexes featuring the Ln^{4+} metal centers. It can be noted that the singly occupied 4f-dominant MO (α spin density, HOMO-20, 69% Pr) of **2-Pr(NP*)** lies significantly deeper in energy (3.03 eV below the HOMO level) than the corresponding orbital in the valence isoelectronic **1-Ce(NP*)**, where it was found at the HOMO level. This explains the absence of the f-d transitions in **2-Pr(NP*)**, as opposed to the **1-Ce(NP*)** complex exhibiting the f-d transitions in the 320-370nm range, as expected for the Ce^{3+}, $4f^1$ configuration.

However, it is clear that there is a peak at 400 nm in TDDFT that seems out of place, as well as an overestimation of the 280 nm transition (Fig. 6b). The 280 nm experimental peak is dominated by excitations from the nearly degenerate 1st excited state in XMS-PDFT (Figure S45) and the strongest intensities around 600 nm are also dominated by transitions from the 1st excited state in XMS-PDFT. While the transitions originating from the XMS-DFT ground state seem to be captured with TDDFT (Figure 6B), those that originate from the nearly degenerate state are overestimated. In Figure S49, we show a hypothetical TDDFT spectrum, where the transitions around 200 nm in Fig 6 are red-shifted by 70 nm and those between 360-430 nm with oscillator strength > 0.01 are red-shifted by 215 nm. The hypothetical spectrum is much closer to XMS-PDFT, especially around 600 nm, indicating the failure of conventional TDDFT to capture the electronic transitions of such a multi-reference system.

Looking back at the Tb^{4+} TDDFT spectrum, there is a predicted transition between 300-400nm that is similar to the strong transition found in Pr^{4+} with TDDFT in the same region. Given the insights from XMS-PDFT with Pr^{4+}, the Tb^{4+} spectrum is a good candidate to be revisited with multireference treatment. For **2-Nd(NP*)** and **2-Dy(NP*)**, the spectra are different from **2-Pr(NP*)**, but their Ln–N average bond lengths are much more similar to the **1-Ln(NP*)** series. What sets **2-Pr(NP*)** and **2-Tb(NP*)** apart are that their average Ln–N bond lengths are significantly shorter and more covalent than the **1-Ln(NP*)**, including the isoelectronic (to Pr^{4+}) **1-Ce(NP*)**. It has previously been shown for a series of bimetallic transition metal complexes that the most challenging electronic structure of the series to describe with DFT was the complex with the most covalent bond.[53,54] It seems this could be a similar situation with this family of lanthanide complexes, where the increased covalency of the Pr–N bond in **2-Pr(NP*)** creates a more complicated electronic structure that cannot accurately be described with a single reference method. The multiconfigurational nature of the ground and excited states make **2-Pr(NP*)** a challenging system for TDDFT. With the advent of MC-PDFT and XMS-PDFT, it is now possible to use wave function theory at an affordable cost for larger systems, minimizing the need to rely on single reference methods that may give correct energies, but may have an incomplete or wrong description of the character of the states.

Conclusions

The tetravalent oxidation state of praseodymium in an imidophosphorane complex is observed in solution and characterized by cyclic voltammetry, UV-vis-NIR and X-band EPR spectroscopy, and supported by theoretical modeling. The imidophosphorane ligand, $[NP^*]^{1-}$, effectively shifts the $Pr^{3+/4+}$ redox couple to a window that is accessible with mild oxidants such as AgI and I_2. Despite the redox accessibility of Pr^{4+} (at -0.72 V vs. Fc/Fc^+), the species generated through chemical and electrochemical oxidation is not stable at -35 ˚C or above. This reactivity is similar to that of $[Pr^{4+}(OSiPh_3)_4(MeCN)_2]$, which is also thermally unstable, at room temperature in solution, but isolable. The moderate changes in stability between **2-Pr(NP*)** and $[Pr^{4+}(OSiPh_3)_4(MeCN)_2]$, despite relatively mild reduction potentials for both complexes, indicate that the nature of the ligand field and its solubility, steric profile, and crystallization dynamics are all crucial contributing factors that influence solution and solid-state stability. Additionally, it is clear that redox accessibility does not correlate directly with the ability to isolate a complex. In fact, in this series of complexes the tetravalent end members, **2-Ce(NP*)** and **2-Tb(NP*)** are both isolable and readily crystallized. In the case of **2-Pr(NP*)** there are subsequent competing reactions that complicate isolation, but pose an intriguing challenge for further ligand development.

This study is a crucial component of understanding molecular tetravalent lanthanide chemistry as it reports the first CW X-band EPR study of this key $4f^1$ ion. This spectroscopic measurement enables comparison with lanthanide and actinide f^1 analogs and maps both effects of changes in the magnitude of crystal field and spin-orbit coupling. In contrast to Ce^{3+}, Pr^{4+} complexes are expected to diverge with increased crystal electric field. Therefore, this measurement and the large observed A values (which match previous solid-state measurements)[6,40–46] indicate significant changes in the fundamental single-ion properties in the tetravalent state in comparison to the trivalent for the lanthanides series.[55]

The *in situ* characterization of the tetravalent oxidation state for **2-Pr(NP*)** by EPR and UV-vis spectroscopy is substantially supported by comprehensive theoretical modeling including both DFT and multi-reference methods. The interrogation of Nd^{3+} and Dy^{3+} complexes establishes periodic redox properties and demonstrates the nature of ligand involvement in redox events providing design parameters for stabilizing tetravalent lanthanides. Based on the PBE0-computed MO energy levels of the Ln^{3+} species **1-Ln(NP*)** (Ln=Pr, Nd, Tb, Dy), transition from metal-centered to ligand-centered oxidation for these complexes occurs when the highest occupied 4f dominant MO of Ln is between 0.65 and 0.85 eV from the HOMO level. This observation can used as a guideline for future studies of similar complexes of other Ln metals. For systems with complex electronic structures, it is critical to evaluate their multiconfigurational behavior which may be essential to correctly simulate their optical properties in the future studies.

Author Contributions

N.T. R. and I.A.P. contributed equally to this work.

Conflicts of interest

There are no conflicts to declare.

Acknowledgements

This material is based upon work supported by Georgia Institute of Technology and NSF grant CHE-1943452. Single-crystal

diffraction experiments were performed at the GT SC-XRD facility directed by J.B. X-Band EPR spectra were obtained at the National High Magnetic Field laboratory under proposal number P19275 and with the help of Dr. Likai Song. I.A.P. is supported by a J. Robert Oppenheimer Distinguished Postdoctoral Fellowship at Los Alamos National Laboratory. S.M.G. acknowledges support from a Director's Postdoctoral Fellowship (LANL-LDRD). R.K.C., E.R.B. and P.Y. are supported by the Heavy Element Chemistry Program sponsored by the Division of Chemical Sciences, Geosciences, and Biosciences, Office of Basic Energy Sciences, U.S. Department of Energy, at Los Alamos National Laboratory (LANL). LANL is operated by Triad National Security, LLC, for the National Nuclear Security Administration of U.S. Department of Energy (Contract No. 89233218CNA000001).

Notes and references

‡ CCDC 1992310, 2114480, and 2115069 contain the supplementary crystallographic data for this paper. These data can be obtained free of charge via www.ccdc.cam.ac.uk/structures, or by emailing data_request@ccdc. cam.ac.uk, or by contacting The Cambridge Crystallographic Data Centre, 12 Union Road, Cambridge CB2 1EZ, UK; fax: +44 1223 336033.

† The measured potentials demonstrated a sensitivity to the scan window range. All scan windows were thus kept the same to allow for a better comparison of reported potentials.

1 N. T. Rice, I. A. Popov, D. R. Russo, J. Bacsa, E. R. Batista, P. Yang, J. Telser and H. S. La Pierre, *J. Am. Chem. Soc.*, 2019, **141**, 13222–13233.

2 C. T. Palumbo, I. Zivkovic, R. Scopelliti and M. Mazzanti, *J. Am. Chem. Soc.*, 2019, **141**, 9827–9831.

3 A. R. Willauer, C. T. Palumbo, R. Scopelliti, I. Zivkovic, I. Douair, L. Maron and M. Mazzanti, *Angew. Chemie Int. Ed.*, 2020, **59**, 3549–3553.

4 A. R. Willauer, C. T. Palumbo, F. Fadaei-Tirani, I. Zivkovic, I. Douair, L. Maron and M. Mazzanti, *J. Am. Chem. Soc.*, 2020, **142**, 5538–5542.

5 N. T. Rice, I. A. Popov, D. R. Russo, T. P. Gompa, A. Ramanathan, J. Bacsa, E. R. Batista, P. Yang and H. S. La Pierre, *Chem. Sci.*, 2020, **11**, 6149–6159.

6 T. P. Gompa, A. Ramanathan, N. T. Rice and H. S. La Pierre, *Dalt. Trans.*, 2020, **49**, 15945–15987.

7 A. R. Willauer, I. Douair, A.-S. Chauvin, F. Fadaei Tirani, J.-C. G. Bunzli, L. Maron and M. Mazzanti, *Chem. Sci.*, , DOI:10.1039/D1SC05517H.

8 C. Thibault and S. E. J., *Science*, 2019, **363**, 489–493.

9 K. L. Nash, *Solvent Extr. Ion Exch.*, 1993, **11**, 729–768.

10 K. L. Nash and J. C. Braley, in *Nuclear Energy and the Environment*, American Chemical Society, 2010, vol. 1046, pp. 3–19.

11 C. A. Gould, K. R. McClain, J. M. Yu, T. J. Groshens, F. Furche, B. G. Harvey and J. R. Long, *J. Am. Chem. Soc.*, 2019, **141**, 12967–12973.

12 K. R. Meihaus, M. E. Fieser, J. F. Corbey, W. J. Evans and J. R. Long, *J. Am. Chem. Soc.*, 2015, **137**, 9855–9860.

13 H. S. La Pierre, H. Kameo, D. P. Halter, F. W. Heinemann and K. Meyer, *Angew. Chemie Int. Ed.*, 2014, **53**, 7154–7157.

14 M. R. MacDonald, M. E. Fieser, J. E. Bates, J. W. Ziller, F. Furche and W. J. Evans, *J. Am. Chem. Soc.*, 2013, **135**, 13310–13313.

15 F.-S. Guo, N. Tsoureas, G.-Z. Huang, M.-L. Tong, A. Mansikkamäki and R. A. Layfield, *Angew. Chemie Int. Ed.*, 2020, **59**, 2299–2303.

16 M. A. Hay and C. Boskovic, *Chem. – A Eur. J.*, 2021, **27**, 3608–3637.

17 L. J. Nugent, R. D. Baybarz, J. L. Burnett and J. L. Ryan, *J. Inorg. Nucl. Chem.*, 1971, **33**, 2503–2530.

18 S. Cotton, *Lanthanide and Actinide Chemistry*, Wiley & Sons Ltd., West Sussex, England, 2006.

19 L. R. Morss, *Chem. Rev.*, 1976, **76**, 827–841.

20 T. Vent-Schmidt and S. Riedel, *Inorg. Chem.*, 2015, **54**, 11114–11120.

21 T. Vent-Schmidt, Z. Fang, Z. Lee, D. Dixon and S. Riedel, *Chem. – A Eur. J.*, 2016, **22**, 2406–2416.

22 T. Mikulas, M. Chen, D. A. Dixon, K. A. Peterson, Y. Gong and L. Andrews, *Inorg. Chem.*, 2014, **53**, 446–456.

23 A. F. Lucena, C. Lourenço, M. C. Michelini, P. X. Rutkowski, J. M. Carretas, N. Zorz, L. Berthon, A. Dias, M. Conceição Oliveira, J. K. Gibson and J. Marçalo, *Phys. Chem. Chem. Phys.*, 2015, **17**, 9942–9950.

24 S. P. Willson and L. Andrews, *J. Phys. Chem. A*, 1999, **103**, 3171–3183.

25 J. Su, S. Hu, W. Huang, M. Zhou and J. Li, *Sci. China Chem.*, 2016, **59**, 442–451.

26 B. Monteiro, N. A. G. Bandeira, C. Lourenço, A. F. Lucena, J. M. Carretas, J. K. Gibson and J. Marçalo, *Chem. Commun.*, 2019, **55**, 14139–14142.

27 S.-X. Hu, J. Jian, J. Su, X. Wu, J. Li and M. Zhou, *Chem. Sci.*, 2017, **8**, 4035–4043.

28 Q. Zhang, S.-X. Hu, H. Qu, J. Su, G. Wang, J.-B. Lu, M. Chen, M. Zhou and J. Li, *Angew. Chemie Int. Ed.*, 2016, **55**, 6896–6900.

29 P. D. Dau, M. Vasiliu, K. A. Peterson, D. A. Dixon and J. K. Gibson, *Chem. – A Eur. J.*, 2017, **23**, 17369–17378.

30 D. E. Hobart, J. P. Young, V. E. Norvell, G. Mamantov, J. R. Peterson and K. Samhoun, *Inorg Nucl Chem Lett*, 1980, **16**, 321–328.

31 M. Gregson, E. Lu, D. P. Mills, F. Tuna, E. J. L. McInnes, C. Hennig, A. C. Scheinost, J. McMaster, W. Lewis, A. J. Blake, A. Kerridge and S. T. Liddle, *Nat. Commun.*, 2017, **8**, 14137.

32 T. P. Gompa, N. T. Rice, D. R. Russo, L. M. Aguirre Quintana, B. J. Yik, J. Bacsa and H. S. La Pierre, *Dalt. Trans.*, 2019, **48**, 8030–8033.

33 R. Shannon, *Acta Crystallograpica Sect. A*, 1976, **32**, 751–767.

34 N. A. Piro, J. R. Robinson, P. J. Walsh and E. J. Schelter, *Coord. Chem. Rev.*, 2014, **260**, 21–36.

35 J. R. Robinson, P. J. Carroll, P. J. Walsh and E. J. Schelter, *Angew. Chemie Int. Ed.*, 2012, **51**, 10159–10163.

36 N. G. Connelly and W. E. Geiger, *Chem. Rev.*, 1996, **96**, 877–910.

37 L. M. Aguirre Quintana, N. Jiang, J. Bacsa and H. S. La Pierre, *Dalt. Trans.*, 2020, **49**, 5420–5423.

38 X. Wang, L. Andrews, Z. Fang, K. S. Thanthiriwatte, M. Chen and D. A. Dixon, *J. Phys. Chem. A*, 2017, **121**, 1779–1796.

39 A. Abragam and B. Bleaney, *Electron Paramagnetic Resonance of Transition Ions*, Oxford University Press, 1970.

40 Y. Hinatsu, *J. Solid State Chem.*, 1996, **122**, 384–389.

41 Y. Hinatsu and N. Edelstein, *J. Solid State Chem.*, 1994, **112**, 53–57.

42 Y. Hinatsu and N. Edelstein, *J. Alloys Compd.*, 1997, **250**, 400–404.

43 K. Tezuka and Y. Hinatsu, *J. Solid State Chem.*, 1999, **143**, 140–143.

44 E. A. Harris, J. H. Mellor and S. Parke, *Phys. status solidi*, 1984, **122**, 757–760.

45 K. Tezuka and Y. Hinatsu, *J. Solid State Chem.*, 2001, **156**, 203–206.

46 Y. Hinatsu, *J. Solid State Chem.*, 1997, **130**, 250–253.

47 G. Li Manni, R. K. Carlson, S. Luo, D. Ma, J. Olsen, D. G. Truhlar and L. Gagliardi, *J. Chem. Theory Comput.*, 2014, **10**, 3669–3680.

48 J. J. Bao, C. Zhou, Z. Varga, S. Kanchanakungwankul, L. Gagliardi and D. G. Truhlar, *Faraday Discuss.*, 2020, **224**, 348–372.

49 R. K. Carlson, D. G. Truhlar and L. Gagliardi, *J. Chem. Theory Comput.*, 2015, **11**, 4077–4085.

50 M. Tricoire, N. Mahieu, T. Simler and G. Nocton, *Chem. – A Eur. J.*, 2021, **27**, 6860–6879.

51 M. D. Walter, C. H. Booth, W. W. Lukens and R. A. Andersen, *Organometallics*, 2009, **28**, 698–707.

52 D.-C. Sergentu, C. H. Booth and J. Autschbach, *Chem. – A Eur. J.*, 2021, **27**, 7239–7251.

53 S. J. Tereniak, R. K. Carlson, L. J. Clouston, V. G. Young, E. Bill, R. Maurice, Y.-S. Chen, H. J. Kim, L. Gagliardi and C. C. Lu, *J. Am. Chem. Soc.*, 2014, **136**, 1842–1855.

54 R. K. Carlson, S. O. Odoh, S. J. Tereniak, C. C. Lu and L. Gagliardi, *J. Chem. Theory Comput.*, 2015, **11**, 4093–4101.

55 M. J. Daum, A. Ramanathan, A. I. Kolesnikov, S. Calder, M. Mourigal and H. S. La Pierre, *Phys. Rev. B*, 2021, **103**, L121109.